Three-dimensional finite element method for rotating disk flows

G. R. Anjos, N. Mangiavacchi & J. Pontes

Springer

Springer

TECHNICAL PAPER

Three-dimensional finite element method for rotating disk flows

G. R. Anjos · N. Mangiavacchi · J. Pontes

Abstract This paper deals with the numerical simulation of rotating disk flow, coupling the hydrodynamic field to the transport of a chemical species generated in electrochemical cells by the dissolution of an iron electrode in a 1M H_2SO_4 electrolyte. The time asymptotic steady-state solution of rotating disk flow obtained in this work by numerical integration of the incompressible Navier–Stokes equations through the finite element method (FEM) with the appropriate boundary conditions is consistent with the generalized von Kármán's similarity solution. This paper reviews the main features of generalized von Kármán's flow, the adopted FEM scheme, a discussion of implementation of the boundary conditions, validation of the code and the results. In particular, the results confirm the assumption that the non-dimensional velocity and concentration profiles do not depend on the coordinate along the radial direction.

Keywords Finite element method · Semi-Lagrangian method · Rotating disk flow · Transition to turbulence · Electrochemistry · Corrosion

G. R. Anjos (✉) · N. Mangiavacchi
Group of Environmental Studies for Water Reservoirs, GESAR,
State University of Rio de Janeiro, R. Fonseca Telles 524,
Rio de Janeiro, RJ 20550-013, Brazil
e-mail: gustavo.rabello@gmail.com; rabello@mit.edu

N. Mangiavacchi
e-mail: norberto@uerj.br

J. Pontes
Metallurgy and Materials Engineering Department,
PEMM/COPPE/UFRJ, P.O. Box 68505, Rio de Janeiro,
RJ 21941-972, Brazil
e-mail: jopontes@metalmat.ufr.br

1 Introduction

Rotating disk flows belong to the restricted class of problems having a similarity semi-analytical solution of the hydrodynamic equations. The angular velocity of the disk and the non-vanishing fluid viscosity led to the development of a boundary layer where the velocity field encompasses an azimuthal component, which decreases from the disk velocity at the interface, to zero outside the boundary layer. A secondary radial flow induced by centrifugal effect and an incoming radial flow approaching the disk surface to match the continuity requirement complete the description of the velocity field. The semi-analytical solution of this three-dimensional flow was found by von Kármán (see [1]).

Rotating disk flow occurs in a class of electrochemical cells. Cells comprising a rotating disk electrode are widely used due to the rather simple setup and to the fact that the mass flow because of the dissolution of the electrode in the electrolyte acid medium is independent of the radial position at the interface. Figure 1 schematically shows the typical setup of an electrochemical cell with three electrodes here considered. The counter electrode consists of a platinum screen placed along the cell walls to assure a uniform distribution of the electric potential in the system. The working electrode is made of an iron rod with a diameter of 5 mm, covered with a 2.5-mm-thick epoxy coating except at the electrode base, through where the current flows. The working electrode is coupled to an adjustable angular velocity motor. Typical angular velocities range from 100 to 900 rpm. The electric current in the cell is produced by the ions transfer at the electrode/electrolyte interface, which depends on two effects: interfacial concentration gradient ($i \propto dC/dz|_{z=0}$) of ions and migration due to the electric field. Barcia et al. [2] showed that

Fig. 1 Scheme of typical electrochemical cell with a rotating disk electrode and the associated polarization curve, with the three regions. First region: the current depends only on the applied voltage. Second region: the current depends on both the applied voltage and the angular velocity imposed to the rotating disk electrode. Third region: the current depends only on the angular velocity, namely on the hydrodynamics close to the disk

(a)   (b)
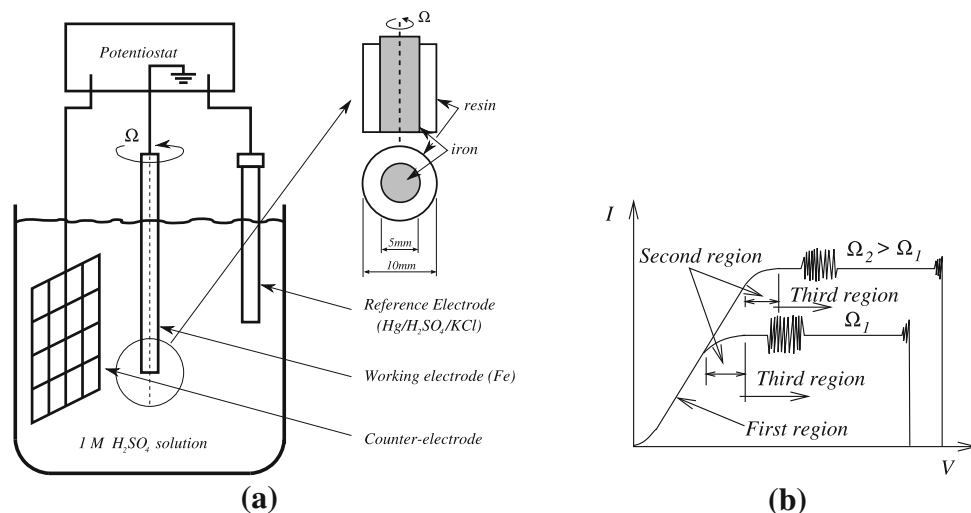
the first one dominates the process, leading to the conclusion that the current depends on the spatial distribution of the relevant electrically charged chemical species. An oscillation of the hydrodynamic field and of the interfacial gradient of the relevant chemical species could, thus, drive current oscillations.

Polarization curves experimentally obtained in the electrodissolution of iron electrodes in 1M solutions of H_2SO_4 present a plateau [2], where the current is independent of the applied overvoltage and depends on the electrode angular velocity Ω, which, in turn, affects the hydrodynamics of the system. Consequently, the current is controlled by the hydrodynamics; the characteristic overvoltage plateau level is proportional to $\Omega^{1/2}$.

Dissolution of the electrode gives rise to a thin mass concentration boundary layer due to a Schmidt number $Sc = 2{,}000$. Thickness of thin mass boundary layer is of order of 5 % of the thickness of the hydrodynamic one. In addition, dependency of the flow viscosity on the mass concentration field couples both fields and results in a rotating disk flow substantially less stable than flows developed with constant viscosity [3]. In particular, Mangiavacchi et al. [3] found a unstable oscillation of the concentration gradient at the electrode interface, at distances from the axis (Reynolds numbers) of order of the electrode diameter. The result reinforces the hypothesis about the hydrodynamic origin of the current oscillation found at the plateau of the polarization curve (see Fig. 1). The stability results obtained by Mangiavacchi et al. [3] motivate our group to develop a finite element code suitable for direct numerical simulation (DNS) of rotating disk flow in electrochemical cells and pursue the stability study of the coupled fields and investigate the system behavior in the non-linear region.

The FEM has been used, since the 1950s, in solid mechanics to solve problems which the available standard

methods were not capable of handling. Only later on, in the 1970s, the FEM began to be used to discretize the governing equations in fluid dynamics, mostly due to the consolidation of the Galerkin method for the diffusion equations. The relatively late start in fluid dynamics is mainly attributed to the strong velocity–pressure coupling and convective terms found in the Navier–Stokes equations, in which the later cannot be written in terms of a linear combination of independent components. Therefore, the non-linearity produces non-symmetric operators whose inversion is not trivial. Moreover, the greater is the Reynolds number Re, the larger is the influence of the convective term in the equations. Another numerical obstacle is the incompressibility condition, which is found in many practical problems. Such a condition imposes that the velocity field must have zero divergence, thus requiring the coupled solution of the pressure field. However, many authors have started to develop important tools to investigate these problems and different approaches are found in the basic literature.

One of the main features of the finite element method stands on the choice of the element used to discretize the numerical domain. Moreover, artificial stabilization may be used to avoid lack of stability in certain combination of elements if they fail to discretize functions with the appropriate space requirements. For instance, in [4] and [5], a new Petrov–Galerkin formulation for Stokes problems was derived. The strong Babuska–Brezzi condition was "circumvented" by introducing an artificial stabilization process which allowed the use of elements with the same order to discretize fluid flow equations, therefore reducing considerably the size of the final linear system and, consequently, the time spent to solve it. However, its implementation is not straightforward and the required assembling time may be larger than those found in the standard methods. While this finite element formulation is

J Braz. Soc. Mech. Sci. Eng. (2014) 36:709–724

711

proposed to solve the Stokes problems, it can be successfully applied in the Navier–Stokes equations to avoid function space restrictions commonly found in velocity–pressure coupling problems.

The Taylor–Galerkin method for finite element schemes was proposed and discussed in [6]. The method is described for scalar convection equations in one or more space dimensions, which produces accurate temporal differencing using Taylor series expansions. In Taylor–Galerkin methods, the time discretization plays an important role; therefore, the time-stepping is chosen so that the stabilization occurs in a natural way under certain time step restriction. The method is compared to the Galerkin and Petrov–Galerkin methods and the conclusion is that the new methodology produces high-phase accuracy with very low numerical diffusion.

In [7], a two-step explicit Finite Element scheme was proposed to obtain time-accurate solutions for compressible Euler equations. In addition, an adaptive mesh refinement scheme was proposed to rearrange the elements according to a required accuracy for compressible flows. The computational domain is discretized by tetrahedron elements in an uniform grid and common benchmarks are performed to evaluate the accuracy of the proposed methodology.

In [8] and [9], a discontinuous Galerkin formulation applied to the Finite Element method was studied. The method proposed was able to solve pure diffusion and convection–diffusion problems with different levels of mesh refinement. They performed several stability analysis studies and compared results with the standard continuous Galerkin method, thus demonstrating quantitatively and qualitatively the superiority of the proposed discontinuous formulation against the continuous case.

Numerical simulations of rotating disk flow with constant viscosity were performed, for instance, by Moisy et al. [10], who addressed the problem of the flow developed between two counter-rotating disks. Spatial discretization was performed by spectral methods and a second-order time marching procedure was adopted, with implicit discretization of linear terms and explicit Adams–Bashforth extrapolation of the non-linear terms.

The aim of this article was to provide an accurate description of the governing equations of the rotating disk flow found in electrochemical cells, the main features of the 3-dimensional finite element (FEM) code developed in our group, sensitive analysis of mesh convergence for two stable finite elements, benchmark test cases for non-coupled equations with semi-analytical solution and, finally, the steady-state solution for the coupled fields, in which the fluid viscosity is directly affected by the concentration field.

2 Governing equations

The flow and the mass concentration field obey the hydrodynamic and transport equations, coupled, through the viscosity ([3, 11, 12]). These equations, written in non-dimensional form read:

$$\frac{D\mathbf{v}}{Dt} = -\nabla p + \frac{1}{Re}\nabla \cdot \left[v(\nabla \mathbf{v} + \nabla \mathbf{v}^{\mathrm{T}}) \right] \tag{1}$$

$$\nabla \cdot \mathbf{v} = 0 \tag{2}$$

$$\frac{DC}{Dt} = \frac{1}{ReSc}\nabla \cdot (\mathcal{D}\nabla C). \tag{3}$$

Non-dimensional variables are defined as follows: The variable viscosity and the diffusion coefficient are made non-dimensional with bulk values $\hat{v}_\infty$ and $\hat{D}_\infty$, respectively. Re and Sc stand for the Reynolds and Schmidt numbers, respectively. Lengths and the spatial variables z and r are made non-dimensional with the boundary layer characteristic length $(\hat{v}_\infty/\Omega)^{1/2}$, where $\hat{v}_\infty$ is the dimensional bulk viscosity. In particular, the non-dimensional reference radius $\hat{R}$ of the numerical domain is the Reynolds number:

$$Re = \frac{\hat{R}}{(\hat{v}_\infty/\Omega)^{1/2}}. \tag{4}$$

The non-dimensional concentration C is defined by the relation:

$$\hat{C} = \hat{C}_\infty + (\hat{C}_{\mathrm{s}} - \hat{C}_\infty)C(z), \tag{5}$$

where $\hat{C}_{\mathrm{s}}$ and $\hat{C}_\infty$ stand for the dimensional concentration of the relevant chemical species at the electrode interface and in the bulk. These equations are complemented by the constitutive equation:

$$v = \exp(mc), \tag{6}$$

In the above equation, v is the non-dimensional viscosity, defined by $\hat{v}/\hat{v}_\infty$, where $\hat{v}$ and $\hat{v}_\infty$ are the dimensional viscosity at a given position and far from the electrode, c is the non-dimensional concentration of the relevant chemical species responsible for the current and affecting the fluid viscosity and m is a parameter that ultimately defines the ratio of the interfacial to the bulk viscosity. The parameter was evaluated based on electrochemical data and led to a ratio $\hat{v}_0/\hat{v}_\infty = 2.255$ [3], where $\hat{v}_0$ is the dimensional viscosity at the disk interface. The diffusion coefficient and the fluid viscosity are related through the Stokes–Einstein equation [1].

$$\mathcal{D}\hat{v} = \hat{\mathcal{D}}_\infty \hat{v}_\infty \tag{7}$$

or, in non-dimensional form:

$$\mathcal{D}v = 1 \tag{8}$$

2.1 von Kármán's generalized steady flow in electrochemical cells

The steady solution of the coupled hydrodynamic and mass concentration fields in electrochemical cells is the von Kármán similarity solution for a fluid with the viscosity depending on the concentration field, which is assumed to vary along the axial coordinate only. We briefly review Mangiavacchi's solution for the sake of completeness. First, a generalization of von Kármán's solution for rotating disk is assumed, in the form:

$$\begin{pmatrix} \hat{v}_r \\ \hat{v}_\theta \\ \hat{v}_z \\ \hat{p} \\ \hat{\mathcal{C}} \end{pmatrix} = \begin{pmatrix} \hat{r}\Omega F(z) \\ \hat{r}\Omega G(z) \\ (\hat{v}_\infty \Omega)^{1/2} H(z) \\ \hat{\rho}\hat{v}_\infty \Omega P(z) \\ \hat{\mathcal{C}}_\infty + \left(\hat{\mathcal{C}}_s - \hat{\mathcal{C}}_\infty\right) C(z) \end{pmatrix}. \tag{9}$$

Dimensional variables in Eq. (9) are denoted with a hat, except for the angular velocity Ω. Boundary conditions for F, G, H and P are $F = H = P = 0$ and $G = 1$ at the disk surface ($z = 0$), $F = H' = 0$ and $G = 0$ as $z \longrightarrow \infty$. The non-dimensional concentration profile, C, varies from 1, at $z = 0$, to 0, as $z \longrightarrow \infty$.

Introducing Eq. (9) and the constitutive equations of the stress tensor with variable viscosity in the hydrodynamic and mass transport equations, together with Eqs. (6) and (7), we obtain the ordinary non-linear system for the axial profiles F, G, H, P and C:

$$2F + H' = 0 \tag{10}$$

$$F^2 - G^2 + HF' - vF'' - v'F' = 0 \tag{11}$$

$$2FG + HG' - vG'' - v'G' = 0 \tag{12}$$

$$P' + HH' - vH'' - 2v'H' = 0 \tag{13}$$

$$ScHC' - \frac{C''}{v} + \frac{v'}{v^2}C' = 0 \tag{14}$$

where prime denotes derivatives with respect to the non-dimensional axial coordinate z. The viscosity v and its derivatives are written in non-dimensional form in the above equations, and:

$$v' = m\exp(mC)C'. \tag{15}$$

The non-dimensional velocity, concentration, viscosity and diffusion coefficient profiles, F, G, H, C, v and $\mathcal{D}$, obtained for $\hat{v}_0/\hat{v}_\infty = 2.255$ and $Sc = 2{,}000$ are shown in Fig. 2.

The thin concentration boundary layer results in velocity profiles very close to the ones obtained for the constant viscosity case. In particular, we obtain $H = -0.88559$ [3] far from the disk for the variable viscosity flow considered, a figure slightly different from the asymptotic value for the constant viscosity case, $H = -0.88447$.

3 Solution of the time-dependent 3-dimensional governing equations

The Eqs. (1–3) with the conditions posed by Eqs. (6–8) were solved by the FEM. A summary of the underlying principles and further details are presented as follows.

Fig. 2 Stationary dimensionless profiles for $Sc = 2{,}000$. **a** Velocity profiles, F, G and H, **b** concentration C, **c** viscosity $v_0/v_\infty = 2.255$ and **d** diffusion D
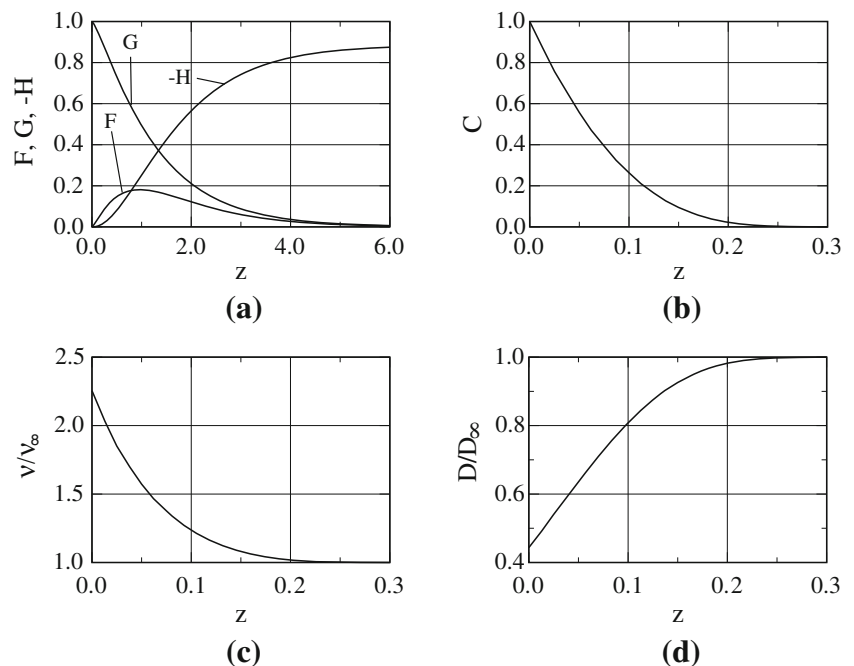
The node distributions in the numerical mesh are a key factor to achieve good accuracy. Due to the complexity of the flow field and the difference between velocity and mass concentration boundary layer thicknesses, the numerical mesh may be more dense close to the working electrode, see Fig. 3a, to assure the accuracy of the simulation. The thickness of element layers progressively increase beyond $z = 0.5$, which is a distance safely out of the concentration boundary layer. To avoid interpolations and losses of accuracy while post-processing the numerical solution along the z axis, the radial point distribution is uniform and it is governed by trigonometric functions, i.e., sine and cosine (see Fig. 3b). With such an approach, the values of the boundary layers F, G, H and C are taken exactly at a mesh node for constant X and Y and variable Z. The domains height extends up to a non-dimensional distance from the electrode surface $z = 10$. The domain radius R defines the Reynolds number of the problem and the value $Re = 100$ was adopted in the present work.

3.1 Implementation of the FEM scheme

The classical Galerkin method [13] was applied to the variational form of the governing equations to discretize all terms except the non-linear convective term. To overcome the obstacle of modeling and implementing a numerical scheme for this term, we employed the semi-Lagrangian technique, which improves the overall stability and allows larger time steps. The two discretization methods are described as follows.

3.2 The Galerkin method

Let us consider the momentum equation in its variational non-dimensional form coupled in the orthogonal directions x, y and z:
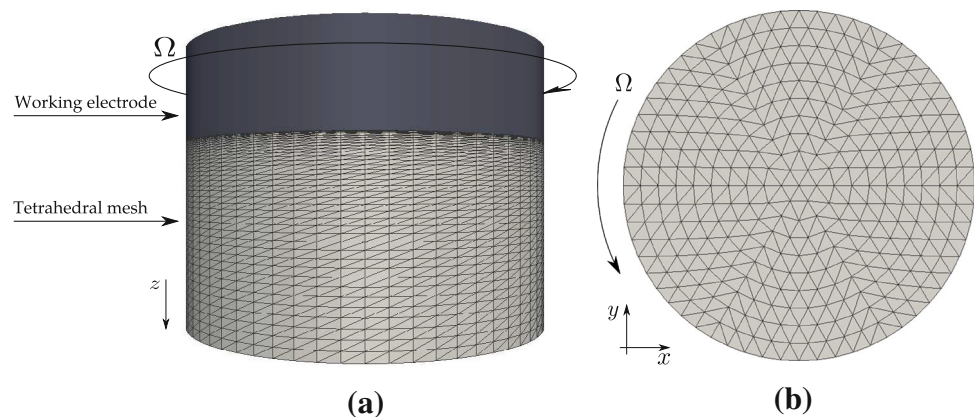
$$\int_\Omega \left[\frac{Du}{Dt} w_x + \frac{Dv}{Dt} w_y + \frac{Dw}{Dt} w_z \right] d\Omega$$
$$- \frac{1}{\rho} \int_\Omega \left[p \frac{\partial w_x}{\partial x} + p \frac{\partial w_y}{\partial y} + p \frac{\partial w_z}{\partial z} \right]$$
$$+ \frac{1}{Re} \int_\Omega \mu \left\{ \left(\frac{\partial u}{\partial x} \frac{\partial w_x}{\partial x} + \frac{\partial v}{\partial x} \frac{\partial w_y}{\partial x} + \frac{\partial w}{\partial x} \frac{\partial w_z}{\partial x} + \frac{\partial u}{\partial y} \frac{\partial w_x}{\partial y} \right. \right.$$
$$+ \frac{\partial v}{\partial y} \frac{\partial w_y}{\partial y} + \frac{\partial w}{\partial y} \frac{\partial w_z}{\partial y} + \frac{\partial u}{\partial z} \frac{\partial w_x}{\partial z} + \frac{\partial v}{\partial z} \frac{\partial w_y}{\partial z} + \frac{\partial w}{\partial z} \frac{\partial w_z}{\partial z} \right)$$
$$+ \left(\frac{\partial u}{\partial x} \frac{\partial w_x}{\partial x} + \frac{\partial u}{\partial y} \frac{\partial w_y}{\partial x} + \frac{\partial u}{\partial z} \frac{\partial w_z}{\partial x} + \frac{\partial v}{\partial x} \frac{\partial w_x}{\partial y} + \frac{\partial v}{\partial y} \frac{\partial w_y}{\partial y} \right.$$
$$\left. \left. + \frac{\partial v}{\partial z} \frac{\partial w_z}{\partial y} + \frac{\partial w}{\partial x} \frac{\partial w_x}{\partial z} + \frac{\partial w}{\partial y} \frac{\partial w_y}{\partial z} + \frac{\partial w}{\partial z} \frac{\partial w_z}{\partial z} \right) \right\} d\Omega = 0$$

(16)

According to the variational formulation, it is required to find the solutions $\mathbf{v} = (u, v, w) \in \mathbb{V}_{\mathbf{v}_\Gamma}$ and $p \in \mathbb{P}$ so that Eq. (16) must be true for all $\mathbf{w} = (w_x, w_y, w_z) \in \mathbb{V}_0$. Note that if the following expressions are satisfied:

$$\int_\Omega \frac{Du}{Dt} w_x d\Omega - \frac{1}{\rho} \int_\Omega p \frac{\partial w_x}{\partial x}$$
$$+ \frac{1}{Re} \int_\Omega \mu \left(\frac{\partial u}{\partial x} \frac{\partial w_x}{\partial x} + \frac{\partial u}{\partial y} \frac{\partial w_x}{\partial y} + \frac{\partial u}{\partial z} \frac{\partial w_x}{\partial z} + \frac{\partial u}{\partial x} \frac{\partial w_x}{\partial x} \right.$$
$$\left. + \frac{\partial v}{\partial x} \frac{\partial w_x}{\partial y} + \frac{\partial w}{\partial x} \frac{\partial w_x}{\partial z} \right) d\Omega = 0$$

(17)

$$\int_\Omega \frac{Dv}{Dt} w_y d\Omega - \frac{1}{\rho} \int_\Omega p \frac{\partial w_y}{\partial y}$$
$$+ \frac{1}{Re} \int_\Omega \mu \left(\frac{\partial v}{\partial x} \frac{\partial w_y}{\partial x} + \frac{\partial v}{\partial y} \frac{\partial w_y}{\partial y} + \frac{\partial v}{\partial z} \frac{\partial w_y}{\partial z} + \frac{\partial u}{\partial y} \frac{\partial w_y}{\partial x} \right.$$
$$\left. + \frac{\partial v}{\partial y} \frac{\partial w_y}{\partial y} + \frac{\partial w}{\partial y} \frac{\partial w_y}{\partial z} \right) d\Omega = 0$$

(18)

Fig. 3 Tetrahedral mesh used on the simulations. **a** Front view of the working electrode and the tetrahedron grid which is placed below the electrode. The points are exponentially distributed from the *top*, where the thin concentration boundary layer requires more points, to the *bottom* of the domain in which the velocity profile is not affected by its boundary layer and the points may be sparsely distributed. **b** Distribution of points on the *x–y* plane

$$\int_\Omega \frac{\mathrm{D}w}{\mathrm{D}t} w_z \mathrm{d}\Omega - \frac{1}{\rho} \int_\Omega p \frac{\partial w_z}{\partial z}$$

$$+ \frac{1}{Re} \int_\Omega \mu \left(\frac{\partial w}{\partial x}\frac{\partial w_z}{\partial x} + \frac{\partial w}{\partial y}\frac{\partial w_z}{\partial y} + \frac{\partial w}{\partial z}\frac{\partial w_z}{\partial z} + \frac{\partial w}{\partial z}\frac{\partial w_z}{\partial x} \right.$$

$$\left. + \frac{\partial w}{\partial z}\frac{\partial w_z}{\partial y} + \frac{\partial w}{\partial z}\frac{\partial w_z}{\partial z} \right) \mathrm{d}\Omega = 0 \tag{19}$$

for any $w_x \in \mathbb{V}_0$, $w_y \in \mathbb{V}_0$ and $w_z \in \mathbb{W}_0$, respectively, then Eq. (16) is automatically satisfied. Therefore, it is possible to solve such an equation by splitting it into the x component [Eq. (17)], the y component [Eq. (18)] and the z component [Eq. (19)] separately, without any loss of generality. The continuity equations is then:

$$\int_\Omega \left(\frac{\partial u}{\partial x} + \frac{\partial v}{\partial y} + \frac{\partial w}{\partial z} \right) q \mathrm{d}\Omega = 0 \tag{20}$$

and the mass transport equation:

$$\int_\Omega \frac{\mathrm{D}c}{\mathrm{D}t} r \mathrm{d}\Omega - \frac{1}{ReSc} \int_\Omega \mathcal{D}\left(\frac{\partial c}{\partial x}\frac{\partial r}{\partial x} + \frac{\partial c}{\partial y}\frac{\partial r}{\partial y} + \frac{\partial c}{\partial z}\frac{\partial r}{\partial z} \right) \mathrm{d}\Omega = 0 \tag{21}$$

Considering NV the number of velocity nodes, NP the number of pressure nodes, Nc the number of concentration nodes and NE the number of finite elements in the discretized domain Ω, the following substitutions in Eq. (16) are required for the Galerkin method:

$$u(\mathbf{x}, t) \approx \sum_{n=1}^{NV} N_n(\mathbf{x}) u_n(t) \tag{22}$$

$$v(\mathbf{x}, t) \approx \sum_{n=1}^{NV} N_n(\mathbf{x}) v_n(t) \tag{23}$$

$$w(\mathbf{x}, t) \approx \sum_{n=1}^{NV} N_n(\mathbf{x}) w_n(t) \tag{24}$$

$$c(\mathbf{x}, t) \approx \sum_{n=1}^{Nc} c_n(\mathbf{x}) c_n(t) \tag{25}$$

$$p(\mathbf{x}, t) \approx \sum_{n=1}^{NP} P_n(\mathbf{x}) p_r(t) \tag{26}$$

which are semi-discrete approximations, i.e., continuous in time (t) and discrete in space ($\mathbf{x}$). Here, $N_n(\mathbf{x})$, $P_n(\mathbf{x})$ and $c_n(\mathbf{x})$ represent velocity, pressure and concentration interpolation functions, respectively.

In the momentum equation, the weight functions w_x, w_y and w_z are replaced by interpolation functions $N_m = N_m(x)$, $m = 1, \ldots, NV$. Therefore, making the suitable substitutions in Eqs. (17, 18 and 21), thus results in:

$$\sum_e \int_{\Omega^e} \sum_n \frac{\mathrm{D}u_n}{\mathrm{D}t} N_m N_n \mathrm{d}\Omega - \sum_e \int_{\Omega^e} \sum_r \frac{\partial N_m}{\partial x} P_r p_r \mathrm{d}\Omega$$

$$+ \frac{1}{Re} \sum_e \int_{\Omega^e} \sum_n \mu^e \left(\frac{\partial N_m}{\partial x}\frac{\partial N_n}{\partial x} u_n + \frac{\partial N_m}{\partial y}\frac{\partial N_n}{\partial y} u_n \right.$$

$$+ \frac{\partial N_m}{\partial z}\frac{\partial N_n}{\partial z} u_n + \frac{\partial N_m}{\partial x}\frac{\partial N_n}{\partial x} u_n + \frac{\partial N_m}{\partial y}\frac{\partial N_n}{\partial x} v_n$$

$$\left. + \frac{\partial N_m}{\partial z}\frac{\partial N_n}{\partial x} v_n \right) \mathrm{d}\Omega = 0 \tag{27}$$

$$\sum_e \int_{\Omega^e} \sum_n \frac{\mathrm{D}v_n}{\mathrm{D}t} N_m N_n \mathrm{d}\Omega - \sum_e \int_{\Omega^e} \sum_r \frac{\partial N_m}{\partial y} P_r p_r \mathrm{d}\Omega$$

$$+ \frac{1}{Re} \sum_e \int_{\Omega^e} \sum_n \mu^e \left(\frac{\partial N_m}{\partial x}\frac{\partial N_n}{\partial x} v_n + \frac{\partial N_m}{\partial y}\frac{\partial N_n}{\partial y} v_n \right.$$

$$+ \frac{\partial N_m}{\partial z}\frac{\partial N_n}{\partial z} v_n + \frac{\partial N_m}{\partial x}\frac{\partial N_n}{\partial y} v_n + \frac{\partial N_m}{\partial y}\frac{\partial N_n}{\partial y} v_n$$

$$\left. + \frac{\partial N_m}{\partial z}\frac{\partial N_n}{\partial y} v_n \right) \mathrm{d}\Omega = 0 \tag{28}$$

$$\sum_e \int_{\Omega^e} \sum_n \frac{\mathrm{D}w_n}{\mathrm{D}t} N_m N_n \mathrm{d}\Omega - \sum_e \int_{\Omega^e} \sum_r \frac{\partial N_m}{\partial z} P_r p_r \mathrm{d}\Omega$$

$$+ \frac{1}{Re} \sum_e \int_{\Omega^e} \sum_n \mu^e \left(\frac{\partial N_m}{\partial x}\frac{\partial N_n}{\partial x} w_n + \frac{\partial N_m}{\partial y}\frac{\partial N_n}{\partial y} w_n \right.$$

$$+ \frac{\partial N_m}{\partial z}\frac{\partial N_n}{\partial z} w_n + \frac{\partial N_m}{\partial x}\frac{\partial N_n}{\partial z} w_n + \frac{\partial N_m}{\partial y}\frac{\partial N_n}{\partial z} w_n$$

$$\left. + \frac{\partial N_m}{\partial z}\frac{\partial N_n}{\partial z} w_n \right) \mathrm{d}\Omega = 0 \tag{29}$$

The mass transport equation does not require high-order elements since there is no coupling with pressure field. The unknown values are computed only at the tetrahedron vertices, thus pairing with the dimension of the unknown values of pressure Nc = NP; however, for better understanding, the dimensions of unknown concentration and pressures will be kept, respectively, as Nc and NP, so that:

$$\sum_e \int_{\Omega^e} \sum_n \frac{\mathrm{D}c_n}{\mathrm{D}t} c_m c_n \mathrm{d}\Omega$$

$$+ \frac{1}{ReSc} \sum_e \int_{\Omega^e} \sum_n k^e \left(\frac{\partial c_m}{\partial x}\frac{\partial c_n}{\partial x} c_n + \frac{\partial c_m}{\partial y}\frac{\partial c_n}{\partial y} c_n \right.$$

$$\left. + \frac{\partial c_m}{\partial z}\frac{\partial c_n}{\partial z} c_n \right) \mathrm{d}\Omega = 0 \tag{30}$$

As mentioned at the beginning of this section, the velocity divergence is strongly linked to the Laplacian of the pressure, thus the continuity equation may be evaluated at the pressure nodes, and therefore, the weight function

q is approximated by the interpolation functions associated to the pressure $P_r(x)$:

$$\sum_e \int_{\Omega^e} \sum_n \left(\frac{\partial N_n}{\partial x} u_n + \frac{\partial N_n}{\partial y} v_n + \frac{\partial N_n}{\partial z} w_n \right) P_r \, d\Omega = 0 \quad (31)$$

for $r = 1, \ldots, \text{NP}$. Restricting the interpolation functions to each element e, it follows that:

$$\sum_e \int_{\Omega^e} \sum_{j,k \in e} \left(\frac{\partial N_j^e}{\partial x} u_j + \frac{\partial N_j^e}{\partial y} v_j + \frac{\partial N_j^e}{\partial z} w_j \right) P_k^e \, d\Omega = 0 \quad (32)$$

Equations (27–30 and 32) may be represented by the system of ordinary differential equations (ODE) below:

$$M_x \dot{u} + \frac{1}{Re} \{ (2K_{xx} + K_{yy} + K_{zz})u$$
$$+ K_{xy} + K_{xz}w \} - G_x p = 0 \quad (33)$$

$$M_x \dot{v} + \frac{1}{Re} \{ K_{yx}u + (K_{xx} + 2K_{yy}$$
$$+ K_{zz})v + K_{yz}w \} - G_y p = 0 \quad (34)$$

$$M_x \dot{w} + \frac{1}{Re} \{ K_{zx}u + K_{zy}v + (K_{xx}$$
$$+ K_{yy} + 2K_{zz})w \} - G_w p = 0 \quad (35)$$

$$D_x u + D_y v + D_z w = 0 \quad (36)$$

$$M_c \dot{c} + \frac{1}{ReSc} (K_{cxx} + K_{cyy} + K_{czz})c = 0 \quad (37)$$

where $\dot{u}, \dot{v}, \dot{w}$ and $\dot{c}$ represent the substantial derivative and are defined as $\dot{u} = [Du_1/Dt, \ldots, Du_{NU}/Dt]^T$, $\dot{v} = [Dv_1/Dt, \ldots, Dv_{NU}/Dt]^T$, $\dot{w} = [Dw_1/Dt, \ldots, Dw_{NV}/Dt]^T$, $\dot{c} = [Dc_1/Dt, \ldots, \partial c_{Nc}/\partial t]^T$, $u = [u_1, \ldots, u_{NU}]^T$, $v = [v_1, \ldots, v_{NV}]^T$, $w = [w_1, \ldots, w_{NV}]^T$, $c = [c_1, \ldots, c_{Nc}]^T$, $p = [p_1, \ldots, p_{NP}]^T$, which are the vectors of nodal values for the velocity, pressure and concentration, respectively. The respective matrix system associated to the ODE's are represented by:

$$\begin{aligned}
M_x &= \mathcal{A}_x(m^e), & M_y &= \mathcal{A}_y(m^e), & M_z &= \mathcal{A}_z(m^e), \\
K_{xx} &= \mathcal{A}_x(k_{xx}^e), & K_{xy} &= \mathcal{A}_x(k_{xy}^e), & K_{xz} &= \mathcal{A}_x(k_{xz}^e), \\
K_{yx} &= \mathcal{A}_y(k_{yx}^e), & K_{yy} &= \mathcal{A}_y(k_{yy}^e), & K_{yz} &= \mathcal{A}_y(k_{yz}^e), \\
K_{zx} &= \mathcal{A}_z(k_{zx}^e), & K_{zy} &= \mathcal{A}_z(k_{zy}^e), & K_{zz} &= \mathcal{A}_z(k_{zz}^e), \\
G_x &= \mathcal{A}_x(g_x^e), & G_y &= \mathcal{A}_y(g_y^e), & G_z &= \mathcal{A}_z(g_z^e), \\
D_x &= \mathcal{A}_x(d_x^e), & D_y &= \mathcal{A}_y(d_y^e), & D_z &= \mathcal{A}_z(d_z^e), \\
K_{cxx} &= \mathcal{A}_x(k_{cxx}^e), & K_{cyy} &= \mathcal{A}_y(k_{cyy}^e), & K_{czz} &= \mathcal{A}_y(k_{czz}^e), \\
& & M_c &= \mathcal{A}_c(m_c^e)
\end{aligned}$$

such that the sub-matrices m^e, k_{xx}^e, k_{xy}^e, k_{xz}^e, k_{yx}^e, k_{yy}^e, k_{yz}^e, k_{zx}^e, k_{zy}^e, k_{zz}^e, g_x^e, g_y^e, g_z^e, d_x^e, d_y^e, d_z^e, m_c^e k_{cxx}^e, k_{cyy}^e and k_{czz}^e are locally defined matrices to each element, so that:

$$m_{ij}^e = \int_{\Omega^e} N_i^e N_j^e \, d\Omega \quad k_{xx,ij}^e = \int_{\Omega^e} v^e \left(\frac{\partial N_i^e}{\partial x} \frac{\partial N_j^e}{\partial x} \right) d\Omega \quad (38)$$

$$k_{xy,ij}^e = \int_{\Omega^e} v^e \left(\frac{\partial N_i^e}{\partial y} \frac{\partial N_j^e}{\partial x} \right) d\Omega \quad k_{xz,ij}^e = \int_{\Omega^e} v^e \left(\frac{\partial N_i^e}{\partial z} \frac{\partial N_j^e}{\partial x} \right) d\Omega \quad (39)$$

$$k_{yx,ij}^e = \int_{\Omega^e} v^e \left(\frac{\partial N_i^e}{\partial x} \frac{\partial N_j^e}{\partial y} \right) d\Omega \quad k_{yy,ij}^e = \int_{\Omega^e} v^e \left(\frac{\partial N_i^e}{\partial y} \frac{\partial N_j^e}{\partial y} \right) d\Omega \quad (40)$$

$$k_{yz,ij}^e = \int_{\Omega^e} v^e \left(\frac{\partial N_i^e}{\partial z} \frac{\partial N_j^e}{\partial y} \right) d\Omega \quad k_{zx,ij}^e = \int_{\Omega^e} v^e \left(\frac{\partial N_i^e}{\partial x} \frac{\partial N_j^e}{\partial z} \right) d\Omega \quad (41)$$

$$k_{zy,ij}^e = \int_{\Omega^e} v^e \left(\frac{\partial N_i^e}{\partial y} \frac{\partial N_j^e}{\partial z} \right) d\Omega \quad k_{zz,ij}^e = \int_{\Omega^e} v^e \left(\frac{\partial N_i^e}{\partial z} \frac{\partial N_j^e}{\partial z} \right) d\Omega \quad (42)$$

$$g_{x,ik}^e = \int_{\Omega^e} \frac{\partial N_i^e}{\partial x} P_k^e \, d\Omega \quad g_{y,ik}^e = \int_{\Omega^e} \frac{\partial N_i^e}{\partial y} P_k^e \, d\Omega \quad (43)$$

$$g_{z,ik}^e = \int_{\Omega^e} \frac{\partial N_i^e}{\partial z} P_k^e \, d\Omega \quad d_{x,kj}^e = \int_{\Omega^e} \frac{\partial N_j^e}{\partial x} P_k^e \, d\Omega \quad (44)$$

$$d_{y,kj}^e = \int_{\Omega^e} \frac{\partial N_j^e}{\partial y} P_k^e \, d\Omega \quad d_{z,kj}^e = \int_{\Omega^e} \frac{\partial N_j^e}{\partial z} P_k^e \, d\Omega \quad (45)$$

$$m_{c,ij}^e = \int_{\Omega^e} N_i^e N_j^e \, d\Omega \quad k_{cxx,ij}^e = \int_{\Omega^e} k^e \left(\frac{\partial c_i^e}{\partial x} \frac{\partial c_j^e}{\partial x} \right) d\Omega \quad (46)$$

$$k_{cyy,ij}^e = \int_{\Omega^e} k^e \left(\frac{\partial c_i^e}{\partial y} \frac{\partial c_j^e}{\partial y} \right) d\Omega \quad k_{czz,ij}^e = \int_{\Omega^e} k^e \left(\frac{\partial c_i^e}{\partial z} \frac{\partial c_j^e}{\partial z} \right) d\Omega \quad (47)$$

The operator $\mathcal{A}$ represents the assembling of elementary sub-matrices of the ODE's system Eq. (37), with respect to the global and local indexes of Eqs. (27–29).

The dimension of the matrices in Eq. (37) is $NV \times NP$ for G_x, G_y and G_z, $NP \times NV$ for D_x, D_y and D_z and $NV \times NV$ for all the remaining matrices. From Eq. (37) it is possible to rewrite the ODE's system in a compact way, coupling the velocities in x, y and z, resulting in:

$$M\dot{\mathbf{v}} + \frac{1}{Re} K\mathbf{v} - Gp = 0 \quad (48)$$

$$D\mathbf{v} = 0 \quad (49)$$

$$M_c\dot{c} + \frac{1}{ReSc}K_c c = 0 \tag{50}$$

where the variables are now defined as $\dot{\mathbf{v}} = [D\mathbf{v}_1/Dt, \ldots, D\mathbf{v}_{NV}/Dt, \quad \mathbf{v}_1, \ldots, \mathbf{v}_{NV}]^T$, $\mathbf{v} = [\mathbf{v}_1, \ldots, \mathbf{v}_{NV}, \mathbf{v}_1, \ldots, \mathbf{v}_{NV}]^T$, $G = [g_1^x, \ldots, g_{NV}^x, g_1^y, \ldots, g_{NV}^y, g_1^z, \ldots, g_{NV}^z]^T$, $D = [d_1^x, \ldots, d_{NV}^x, d_1^y, \ldots, d_{NV}^y, d_1^z, \ldots, d_{NV}^z]^T$, $c = [c_1, \ldots, c_{Nc}]^T$, $\dot{c} = [Dc/Dt, \ldots, Dc_{Nc}/Dt, c, \ldots, c_{Nc}]^T$ and $p = [p_1, \ldots, p_{NP}]^T$, and the matrices as

$$\mathbf{K} = \begin{bmatrix} K_x & K_{yx} & K_{zx} \\ K_{xy} & K_y & K_{zy} \\ K_{xz} & K_{yz} & K_z \end{bmatrix}_{3NV \times 3NV}$$

$$\mathbf{M} = \begin{bmatrix} M_x & 0 & 0 \\ 0 & M_y & 0 \\ 0 & 0 & M_z \end{bmatrix}_{3NV \times 3NV} \qquad \mathbf{G} = \begin{bmatrix} G_x \\ G_y \\ G_z \end{bmatrix}_{3NV \times NP}$$

$$\mathbf{D} = \begin{bmatrix} D_x & D_y & D_z \end{bmatrix}_{NP \times 3NV}$$

$$\mathbf{K_c} = [K_{cxx} + K_{cyy} + K_{czz}]_{Nc \times Nc} \qquad \mathbf{M_c} = [M_c]_{Nc \times Nc}$$

where $K_x = 2K_{xx} + K_{yy} + K_{zz}$, $K_y = K_{xx} + 2K_{yy} + K_{zz}$ and $K_z = K_{xx} + K_{yy} + 2K_{zz}$.

3.3 The semi-Lagrangian method

The semi-Lagrangian method has its own history dating from the end of the 1950s [14] and the beginning of the 1960s [15, 16]. However, the use of such a methodology for modeling fluid flow problems came later in the 1980s through the work of Robert [17] and Pironneau [18], in which predominately convective problems were investigated.

The semi-Lagrangian method was firstly used in convection–diffusion systems where numerical stability and large time steps were required. Since then, this methodology has been shown to fulfill the expectation for large problems to be solved relatively fast. For meteorological purposes, the numerical prediction of weather conditions using the semi-Lagrangian approach has shown to be very effective since large time steps are crucial [19]. The semi-Lagrangian method is not commonly found in the discretization of the Navier–Stokes equations; however, recent works have shown the effectiveness of the semi-Lagrangian method for simulating flows with high velocities [20, 21].

The semi-Lagrangian algorithm is an integrating factor method in which such a factor is an advection operator. This operator is shifted to a moving coordinate system from which the next time step quantity is calculated. Let ψ be a scalar function in its material derivative representation, given in 3-dimensional form as:

$$\frac{D\psi}{Dt} = \frac{\partial\psi}{\partial t} + u\frac{\partial\psi}{\partial x} + v\frac{\partial\psi}{\partial y} + w\frac{\partial\psi}{\partial z} \tag{51}$$

In fluid dynamics, the pure Lagrangian coordinates track the fluid flow by moving the points along its trajectory. However, this may limit the feasible range of simulation conditions, even for low velocity flows, since the particle's trajectory may turn to a chaotic state in a short period of time. Thus, to address such a drawback, the semi-Lagrangian method re-initializes the coordinate system at each time step, consequently recovering the original mesh. The quantity value in the current time step is calculated according to its position in the previous time step, thus this methodology is said to be explicit in time. However, due to its natural description, no time restriction is imposed to satisfy its numerical stability.

Following the description presented above, the Eq. (51) may be discretized linearly in the time domain at the point x_i using an explicit first-order scheme:

$$\frac{D\psi}{Dt} = \frac{\psi_i^{n+1} - \psi_d^n}{\Delta t} \tag{52}$$

where $\psi_d^n = \psi^n(x_d, t^n)$ and x_d is the departure point. In the strong form, the substantial derivative is calculated along the characteristic trajectory, thus finding the point x_d by solving $D\psi/Dt = f$ backwards in time $t^{n+1} \geq t \geq t^n$ using the initial condition $x(t^{n+1}) = x_i$. According to this scheme, the initial position x_i in time t^{n+1} is known and, therefore, it is used to find the departure point x_d, whose position is unknown.

In the semi-Lagrangian context, a searching procedure is required to find the unknown departure points x_d in time t^n. This procedure may lead to excessive computational cost if it is not well designed, thus it should be treated with appropriate care. In this work, this searching procedure is implemented using a smart technique that maps each element node to the opposite element that shares the same face. Therefore, using volume coordinates, it is possible to track the path from the current node's position x_i to its departure point x_d as shown in Fig. 4. As can be seen, only few computational elements are required to find the element in which the departure point is located. Once the point position is known, an interpolation is performed and the quantity is assigned.

Besides the situation described in Fig. 4, many different situations may occur. Figure 5 shows 5 possible trajectories that should be considered while developing the searching procedure. In trajectory 1, the departure point x_d is located near the node position x_i. Once the point's position is found, the interpolated quantity can be assigned. In trajectories 2 and 3, the departure points are located outside the boundary domain. Thus, a boundary element is used to interpolate the quantity to the nodes. Considering trajectories 4 and 5, both cases are similar, however, the searching algorithm in the trajectory 5 demands more computational time; moreover, the trajectory interpolation is less accurate than in trajectory 4.

Above, a summary of the semi-Lagrangian method has been given. It is worth noting that higher accuracy may be achieved if the trajectory is fitted by high-order schemes in time, such as the generalized Adams–Bashforth schemes (see [22]). In the present work, the time restriction limits the displacement of the departure point to one element long, thus a linear approximation of the trajectory achieves reasonable accuracy.

3.4 Semi-Lagrangian method for the Navier–Stokes equations

The procedure described in the previous section is then used to discretize the material derivative of the Navier–Stokes equations. The material derivative in Eq. (53) is substituted into Eq. (1), resulting in:

$$\frac{D\mathbf{v}}{Dt} = \frac{\partial \mathbf{v}}{\partial t} + u\frac{\partial \mathbf{v}}{\partial x} + v\frac{\partial \mathbf{v}}{\partial y} + w\frac{\partial \mathbf{v}}{\partial z} \tag{53}$$

$$\frac{\mathbf{v}_i^{n+1} - \mathbf{v}_d^n}{\Delta t} = -\frac{1}{\rho}\nabla p^{n+1} + \nabla \cdot \left[\mu(\nabla\mathbf{v}^{n+1} + \nabla(\mathbf{v}^{n+1})^{\mathrm{T}})\right] \tag{54}$$

Following the spirit of the semi-Lagrangian discretization method, Eqs. (48–50) are re-written as:

$$m\left(\frac{\mathbf{v}_i^{n+1} - \mathbf{v}_d^n}{\Delta t}, \mathbf{w}\right) - g(p^{n+1}, \mathbf{w}) = 0 \tag{55}$$

$$+\frac{1}{Re}k(v, \mathbf{v}^{n+1}, \mathbf{w}) = 0 \tag{56}$$

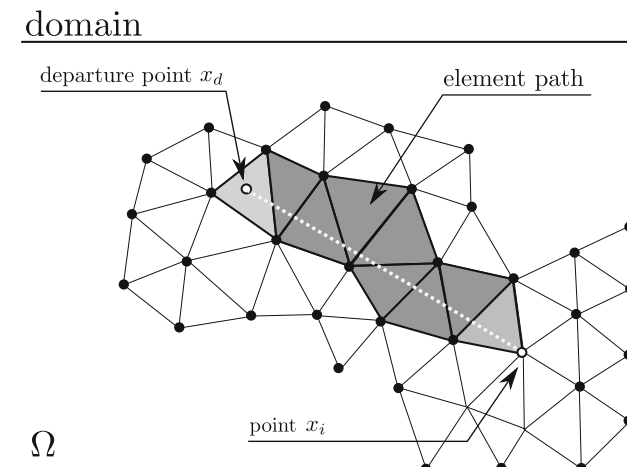$$d(q, \mathbf{v}^{n+1}) = 0, \tag{57}$$

Fig. 4 2-dimensional particle trajectory from the current node's position ψ_i^{n+1} to its corresponding departure point ψ_d^n. The implemented algorithm consists in locating each element backward until the departure point is found. The current state of implementation is first order in space, therefore, the trajectory is approximated by a straight line segment
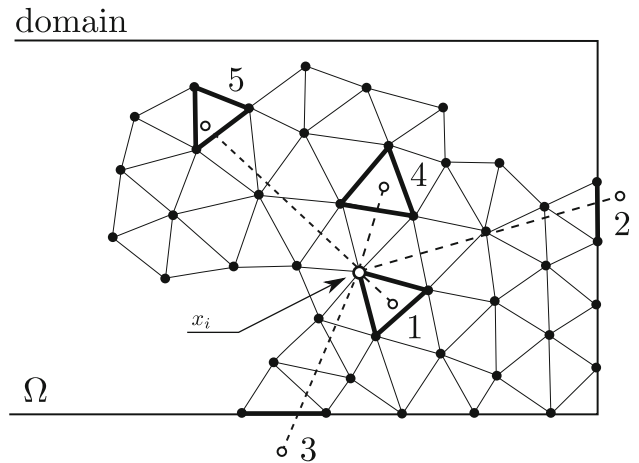

Fig. 5 Interpolation procedures in the semi-Lagrangian method. In trajectories 1, 4 and 5, the departure point ψ_i^{n+1} is located and the Interpolation is thus performed. In trajectories 2 and 3, the departure point is found out of the domain boundary, therefore, only the boundary edges are taken into consideration for the interpolation procedure

$$\tilde{m}_c\left(\frac{c_i^{n+1} - c_d^n}{\Delta t}, r\right) + \frac{1}{ReSc}\tilde{k}_c(\mathcal{D}, c^{n+1}, r) = 0 \tag{58}$$

for all $\mathbf{w} \in \mathbb{V}_0, q \in \mathbb{P}_0$ and $T \in \mathbb{T}_0$. Thus, the resulting discrete matrix form is given by:

$$\begin{array}{rcl} M\left(\frac{\mathbf{v}_i^{n+1} - \mathbf{v}_d^n}{\Delta t}\right) + \frac{1}{Re}K\mathbf{v}^{n+1} - Gp^{n+1} &=& 0 \\ D\mathbf{v}^{n+1} &=& 0 \\ M_c\left(\frac{c_i^{n+1} - c_d^n}{\Delta t}\right) + \frac{1}{ReSc}K_c c^{n+1} &=& 0 \end{array} \tag{59}$$

3.5 3-Dimensional elements

The choice of the appropriate element is a key step to successfully achieve the required precision in the simulations. In fluid dynamics, the element is responsible for the coupling of velocity and pressure and it should satisfy the requirements of the so-called Ladyzhenskaya–Babuska–Brezzi (LBB) stability condition [23–25]. Such a condition imposes the type of velocity and pressure basis functions. One way to avoid the LBB condition is by the use of stabilizing methods such as pressure stabilization, penalty method or artificial compressibility [26, 27]. In this work, LBB-stable elements were chosen. A schematic representation of these elements is shown in Fig. 6 and a short descriptions of their features and their applicability for the Navier–Stokes equation follows.

Linear element: the unknowns are evaluated at the tetrahedron's corners with interpolation functions of order 1. This element is commonly used to solve scalar equations, such as heat and chemical species transport. This element does not satisfy the LBB condition for fluid flow problems

and it cannot be used to solve velocity and pressure without stabilizing methods.

Mini element: this element is part of the Taylor-Hood family and it is a combination of the linear tetrahedron and an additional "bubble" function, built by an additional node localized in its barycenter, thus making it a 5-node element. The interpolation polynomial is of order 4, but it does not present the second and the third degree terms. The pressure is linear and is evaluated at the tetrahedron vertices and the velocity is fourth-order incomplete polynomial and evaluated at all the 5 nodes.

10-node element: defined by additional nodes in the middle of the tetrahedron edges, the 10-node quadratic element is commonly used in fluid flow problems. The interpolation polynomial is of order 2. The pressure is linear and evaluated at the tetrahedron vertices, while the velocity is quadratic and evaluated at all the 10 nodes.

3.6 Projection method

After the spatial and temporal discretization by the FEM, the solution of a set of linear algebraic equations is required. There are many ways to solve this linear system, but due to its size, computational methods may be employed to avoid excessive processing time and memory overhead. The methods for the solution of a linear system may be divided in two groups, namely coupled and uncoupled. The former attempts to solve the complete linear system directly at each time step. However, the direct solution of the Navier–Stokes equations, where pressure and velocity are strongly connected, becomes an onerous procedure. Moreover, the non-linearity of such an equation makes the solution even more complex. Instead, the latter detaches the internal dependencies, allowing a serial resolution of the problem. As part of the uncoupled methods, the projection method has become

popular in the fluid dynamics domain. It was originally introduced by Chorin [28] and thus followed by many others such as Patankar [29] with the SIMPLE method and Harlow and Welch [30] with the MAC method.

The family of projection methods is basically divided into three different parts, namely the continuous projection method, the semi-discrete projection method and the discrete projection method. The projection method in the continuous form attempts to split velocity and pressure before the discretization of the equations is achieved. In the semi-discrete form, the procedure is applied when part of the Navier–Stokes's equation is already discretized in the time domain. The discrete projection method segregates pressure and velocity before the solution of the linear system, thus time and space are already discretized. This work has chosen a variant of the discrete projection method, namely LU-based discrete projection method, and its implementation is formally presented below.

3.7 The LU-based discrete projection method

The discrete projection method based on the LU decomposition is obtained through the factorization of the resulting linear system, so that the velocity and pressure splitting is done after the space and the time discretization:

$$M\left(\frac{\mathbf{v}^{n+1} - \mathbf{v}^n}{\Delta t}\right) + \frac{1}{Re}K\mathbf{v}^{n+1} - Gp^{n+1} = 0 \tag{60}$$

$$D\mathbf{v}^{n+1} = 0 \tag{61}$$

$$M_c\left(\frac{c_i^{n+1} - c_d^n}{\Delta t}\right) + \frac{1}{ReSc}K_c c^{n+1} = 0 \tag{62}$$

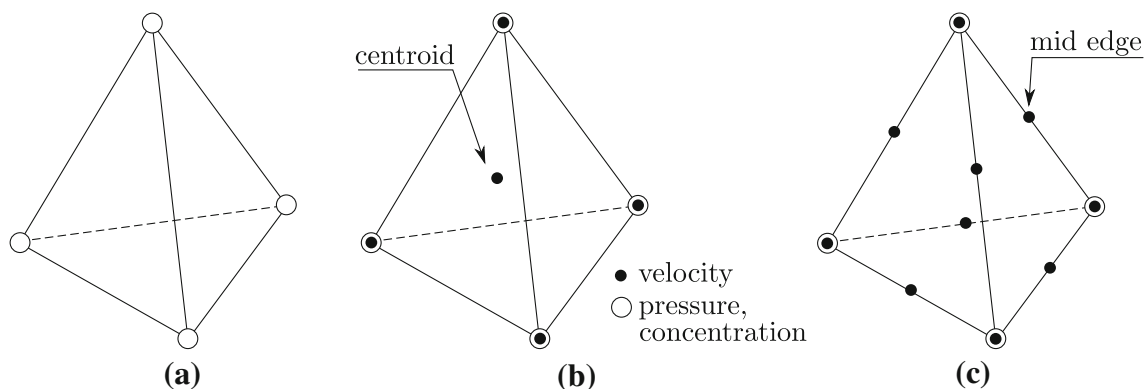Equation (62) can be solved separately, however, Eqs. (60, 61) form a system of equations that may be represented by:

Fig. 6 Schematic representation of 3-dimensional LBB-stable elements used to discretize the finite element domain Ω. **a** Linear element. **b** Mini element, which is a combination of the linear element with an additional node at the element's centroid. Pressure and concentration are evaluated at the element's corners and velocity is computed at the centroid and corners. **c** 10-node element. Additional nodes are placed in the middle of each element edge. Pressure and concentration are evaluated at the corners and velocity is computed at all nodes

$$\begin{bmatrix} B & -\Delta t G \\ D & 0 \end{bmatrix} \cdot \begin{bmatrix} \mathbf{v}^{n+1} \\ p^{n+1} \end{bmatrix} = \begin{bmatrix} r^n \\ 0 \end{bmatrix} + \begin{bmatrix} bc_1 \\ bc_2 \end{bmatrix} \qquad (63)$$

where the system is now written only for the problem unknowns such that $\mathbf{v}^{n+1} = [u_1^{n+1}, \ldots, u_{Nu}^{n+1}, v_1^{n+1}, \ldots, v_{Nv}^{n+1}, w_1^{n+1}, \ldots, w_{Nv}^{n+1}]^T, p^{n+1} = [p_1^{n+1}, \ldots, p_{Np}^{n+1}]^T$, where Nu, Nv, Nw and Np are the number of unknowns for velocity in x, y and z and pressure, respectively. Note that the vector and matrix notation were kept as simple as possible. The $\mathbf{B}$ matrix is given by:

$$B = \frac{M_\rho}{\Delta t} + \frac{K}{Re} \qquad (64)$$

and the right hand side vector stands for the known quantities in current time n,

$$r^n = \frac{M_\rho}{\Delta t} \mathbf{v}_d^n \qquad (65)$$

and the boundary conditions, which are the contributions of known values for velocity and pressure on the right hand side of the system. The projection method based on the LU factorization aims to uncouple the linear system in Eq. (63) through a block factorization. According to Lee et al. [31], such a procedure can be done in several different ways, each one classified by families of methods. Now, consider a LU canonical block factorization as:

$$\begin{bmatrix} B & -\Delta t G \\ D & 0 \end{bmatrix} = \begin{bmatrix} \mathbf{B} & 0 \\ \mathbf{D} & \Delta t \mathbf{D}\mathbf{B_1^{-1}}\mathbf{G} \end{bmatrix} \cdot \begin{bmatrix} \mathbf{I} & -\Delta t \mathbf{B_2^{-1}}\mathbf{G} \\ 0 & \mathbf{I} \end{bmatrix} \qquad (66)$$

Thus, the resulting system is described as:

$$\begin{bmatrix} \mathbf{B} & 0 \\ \mathbf{D} & \Delta t \mathbf{D}\mathbf{B_1^{-1}}\mathbf{G} \end{bmatrix} \cdot \begin{bmatrix} \mathbf{I} & -\Delta t \mathbf{B_2^{-1}}\mathbf{G} \\ 0 & \mathbf{I} \end{bmatrix} \cdot \begin{bmatrix} \mathbf{v}^{n+1} \\ p^{n+1} \end{bmatrix}$$
$$= \begin{bmatrix} r^n \\ 0 \end{bmatrix} + \begin{bmatrix} \mathbf{bc_1} \\ \mathbf{bc_2} \end{bmatrix} \qquad (67)$$

The Uzawa method [32] is achieved if the system presented in Eq. (67) is solved. However, its solution requires the computation of the inverse of matrix $\mathbf{B}$ at each time step, which is a time-consuming task and extremely costly. Such a matrix may be approximated by a diagonal matrix $\mathbf{B_L}$ which is easy and fast to invert. This methodology is known as Matrix Lumping and it has shown to be suitable for the FEM. The main idea of this method is to perform a summation of all entries of a row into its main diagonal. Two diagonalizations were tested, one using the consistent mass matrix $\mathbf{M}$ so that the new approximated diagonal matrix results in $\mathbf{M_L}$, and the second using the matrix $\mathbf{B}$ and resulting in $\mathbf{B_L}$. Both approaches have shown good results, but a small oscillation was noted for the velocity field when the Reynolds number varies from low to moderate values. It is important to note that according to Chang et al. [32], different approximations

can be done for the consistent matrices $\mathbf{B_1}$ and $\mathbf{B_2}$, but to satisfy the continuity equation, it is mandatory that $\mathbf{B_1} = \mathbf{B_2}$, so that all the approximation errors are limited to the momentum equation. Thus, the new uncoupled linear system is described as follows:

$$\begin{bmatrix} \mathbf{B} & 0 \\ \mathbf{D} & \Delta t \mathbf{D}\mathbf{B_1^{-1}}\mathbf{G} \end{bmatrix} \cdot \begin{bmatrix} \tilde{\mathbf{v}}^{n+1} \\ p^{n+1} \end{bmatrix} = \begin{bmatrix} r^n \\ 0 \end{bmatrix} + \begin{bmatrix} \mathbf{bc_1} \\ \mathbf{bc_2} \end{bmatrix} \qquad (68)$$

$$\mathbf{B}\tilde{\mathbf{v}} = \mathbf{r^n} + \mathbf{bc_1} \qquad (69)$$

$$\Delta t \mathbf{D}\mathbf{B^{-1}}\mathbf{G}p^{n+1} = -\mathbf{D}\tilde{\mathbf{v}} + \mathbf{bc_2} \qquad (70)$$

$$\begin{bmatrix} \mathbf{I} & -\Delta t \mathbf{B_2^{-1}}\mathbf{G} \\ 0 & \mathbf{I} \end{bmatrix} \cdot \begin{bmatrix} \mathbf{v}^{n+1} \\ p^{n+1} \end{bmatrix} = \begin{bmatrix} \tilde{\mathbf{v}}^{n+1} \\ p^{n+1} \end{bmatrix} \qquad (71)$$

$$\mathbf{v}^{n+1} = \tilde{\mathbf{v}} + \Delta t \mathbf{B^{-1}}\mathbf{G}p^{n+1} \qquad (72)$$

where t is time and $\mathbf{v}_d^n$ is the velocity calculated in the previous time step at the departure points. Thus, the complete solution procedure is described as follows:

- Compute the trial velocity $\tilde{\mathbf{v}}$ by solving:

  $$\mathbf{B}\tilde{\mathbf{v}} = \mathbf{r^n} + \mathbf{bc_1} \qquad (73)$$

- Compute p^{n+1} from:

  $$\mathbf{D}\mathbf{B_L^{-1}}\mathbf{G}p^{n+1} = -\mathbf{D}(\tilde{\mathbf{v}}_{\mathrm{corr}}) + \mathbf{bc_2} \qquad (74)$$

- Find the solution velocity $\mathbf{v}^{n+1}$ from:

  $$\mathbf{v}^{n+1} = \tilde{\mathbf{v}}_{\mathrm{corr}} + \mathbf{B^{-1}}_L\mathbf{G}p^{n+1} \qquad (75)$$

The subscript L refers to the Lumped matrix, which consists in a diagonal approximation, thus avoiding the computation of the matrix inverse.

3.8 Time step restriction

Despite the stability of large time steps in the semi-Lagrangian methodology, it is important to note that this approach leads to an explicit modeling of the operator, and due to its character, there is no strict time step restriction for its stability. Nevertheless, large time steps should be avoided since the accuracy is first order in time, otherwise important non-linear phenomena may not be captured. The time step constraint for this term is given by the expression below:

$$\Delta t_{sl} < \frac{h_{\min}}{\mathbf{u}_{\max}} \qquad (76)$$

where $h_{\min}$ is the smallest tetrahedral mesh edge length and $\mathbf{u}_{max}$ is the maximum value of velocity given by $\max\{|u|, |v|, |w|\}$.

The two final linear systems in Eqs. (73, 74) are solved at each time step by the conjugate gradient method and the generalized minimum residual method, respectively. The Incomplete Cholesky and LU factorization are used as

720

J Braz. Soc. Mech. Sci. Eng. (2014) 36:709–724

preconditioners to speed up the convergence of the final solution. Once the velocity $\mathbf{v}^{n+1}$ is computed from Eq. (75), the correspondent linear system for the concentration equation is solved at each time step by the conjugate gradient method with the Incomplete Cholesky factorization as preconditioner.

4 Convergence analysis

The analysis of convergence for six different meshes was performed and presented in Fig. 7. The accuracy of the methodology used in this work to compute the solution of the Navier–Stokes equation is evaluated by comparing it to the exact solution of the rotating disk flow for constant viscosity ν. The accuracy of the finite elements used in this work and presented in Sect. 3.5 is evaluated by decreasing the mean tetrahedron edge length size h and the CFL number. Therefore, the convergence of both elements can be accessed. The mean mesh length size h, the total number of nodes and vertices, the CFL number and the total number of elements for each mesh tested in this convergence analysis can be found in Table 1. Note that the difference between the mini and 10-node elements is the total number of nodes, since the total number of vertices and elements are always the same. A convergence to the exact solution of Von Kármán was observed, while the edge length h and CFL decrease as can be seen in Fig. 7. The error is estimated as follows:

$$\mathrm{Error}_{\mathbf{u}} = \sqrt{\frac{\sum(|\mathbf{u}_i - \mathbf{u}_A|)^2}{\sum(|\mathbf{u}_i|)^2}} \tag{77}$$

where $\mathbf{u}$ is the three-component velocity vector for each vertex i in the mesh and $\mathbf{u}_A$ represents the three-component analytical velocity vector. The summation is done varying the z component but keeping the components x and y constant. Note that in this calculation, the nodes belonging to the boundary were not used.

The measurements of convergence were performed assuming the stationary solution when the norm of the error $L_1 < 1E - 06$. Such a norm is assessed through the rate of evolution of the pattern during the simulation by monitoring the relative L_1 norm defined as:

$$L_1 = \frac{1}{\tau} \frac{\sum_{i,j} |u_{i,j}^{n+1} - u_{i,j}^n|}{\sum_{i,j} |u^{n+1}|}, \tag{78}$$

which roughly corresponds to the ratio between the spatial average of the modulus of time derivative u_t and the spatial average of the modulus of the function itself [33]. τ stands for the integration time step.
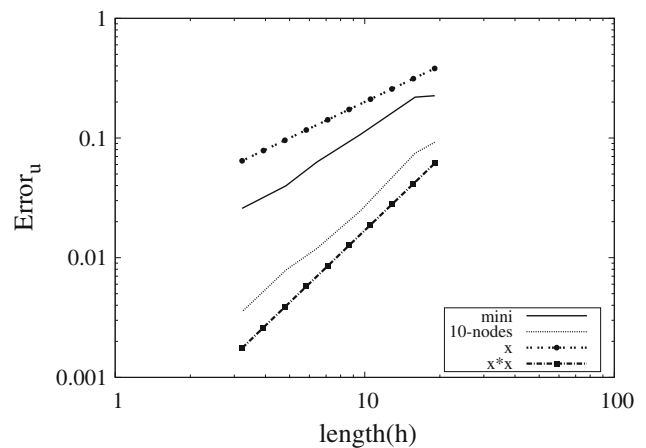

Fig. 7 Mesh convergence analysis for six different meshes. It has been found that the convergence for the mini element at our simulations is of first order, while the 10-node element presented second-order convergence

Table 1 Mesh parameters used in the convergence analysis for the mini and 10-node elements

Mesh	Mean h	CFL	Vertices	Elements	Mini Nodes	10-node
1	19.07	60	910	4,050	4,960	6,289
2	15.90	50	1,524	7,128	8,652	10,787
3	9.613	30	6,620	34,200	40,820	49,179
4	6.431	20	21,630	117,450	139,080	164,669
5	4.829	15	50,440	280,800	331,240	388,759
6	3.224	10	167,460	955,800	1,123,260	1,306,739

4.1 Code validation

In addition to testing the code against standard benchmark problems (Couette-Poiseuille, backward facing step, lid-driven cavity etc.), the code was validated by comparing the results with von Kármán's solution for rotating disk flow with constant viscosity and a generalization for fluids with stratified viscosity depending on the axial coordinate z according to the law:

$$\frac{v_z}{v_\infty} = \frac{v_0}{v_\infty} + \left(1 - \frac{v_0}{v_\infty}\right)\frac{q^{1/3}}{\Gamma(4/3)}\int_0^z e^{-qz^3}\mathrm{d}z. \tag{79}$$

The resulting generalized von Kármán's equations are, in this case [34]:

$$2F + H' = 0 \tag{80}$$

$$F^2 - (G+1)^2 + HF' = \frac{\mathrm{d}}{\mathrm{d}z}\left(\frac{v(z)}{v(\infty)}F'\right) \tag{81}$$

J Braz. Soc. Mech. Sci. Eng. (2014) 36:709–724

721

$$2F(G + 1) + HG' = \frac{d}{dz}\left(\frac{v(z)}{v(\infty)}G'\right) \qquad (82)$$

$$P' + HH' = 2\frac{v'(z)}{v(\infty)}H' + \frac{v(z)}{v(\infty)}H'' \qquad (83)$$

Figure 8a and b shows the non-dimensional F, G and H velocity profiles for the last two cases. In addition to obtaining good agreement with the two above mentioned semi-analytical solutions [34], we found numerical profiles independent of the radial coordinate, an usual assumption made in analytical studies related to rotating disk electrodes.

In addition to the standard numerical benchmark, the code was tested against the non-coupled hydrodynamic field of a rotating disk flow given by the von Kármán's solution [35]. As shown on Fig. 8a, the code was able the recover the analytical steady-state solution after convergence, capturing the thickness of azimuthal, radial and axial boundary layers as well as the correct shape of them. The mesh used in these two benchmarks comprised 97550 vertices, 648800 nodes and 551,250 elements using the LBB-stable mini element.

The stratified non-uniform viscosity problem was treated here in addition to the benchmark tests. The velocity boundary layer thickness increased compared to the previous test case due to higher viscosity profile, shown on Fig. 8b. This result agrees with that reported by Pontes et al. [34].

These results represent the accuracy and stability of the employed method, even for long integration times (CFL $= \Delta t U/\Delta x \approx 5$), and not presenting spurious oscillations even for elevated Reynolds and Schmidt values.

5 Results

This section reviews the semi-analytical profiles of the steady hydrodynamic and mass concentration fields in an electrochemical cell obtained by Mangiavacchi et al. [3] and the profiles obtained for the coupled fields with the FEM code written according to the methods described in this paper.

5.1 FEM-DNS of the base state in electrochemical cells

A cylindrical Cartesian mesh was used as computational domain to simulate the flow field, as shown previously in Fig. 3. The rotating disk was placed on the top of the domain along the x and y coordinates, assuming the angular velocity Ω equal to the unity. The pressure was set on the circular side wall as a standard outflow boundary condition and the velocity components u, v and w were prescribed as inflow on the bottom part fulfilling the discretization of the 3-dimensional Navier–Stokes's equations requirements as follows:

$$X = -Y * \Omega \quad Y = X * \Omega \quad Z = 0 \qquad (84)$$

By considering the numerical domain sufficiently larger than the boundary layer thickness, we can assume $u = v = 0$ on the bottom of the numerical domain. Concerning the axial component w of the velocity, we assumed the value obtained by integration of the generalized von Kármán equations, in order to minimize lateral recirculation effects that appear in consequence of a finite domain.

Due to the boundary conditions setup it is important to highlight the flexibility of the discretization method to represent any type of electrode geometry. The parameters used to simulate this case were: $Re = 100$, $Sc = 2000$, non-dimensional density $\rho = 1$ and viscosity $v = 1$. The results presented in Sect. 2.1 were used to validate the FEM-DNS code.

It can be seen in Fig. 9 that the transient state of the velocity and concentration boundary layers shows an
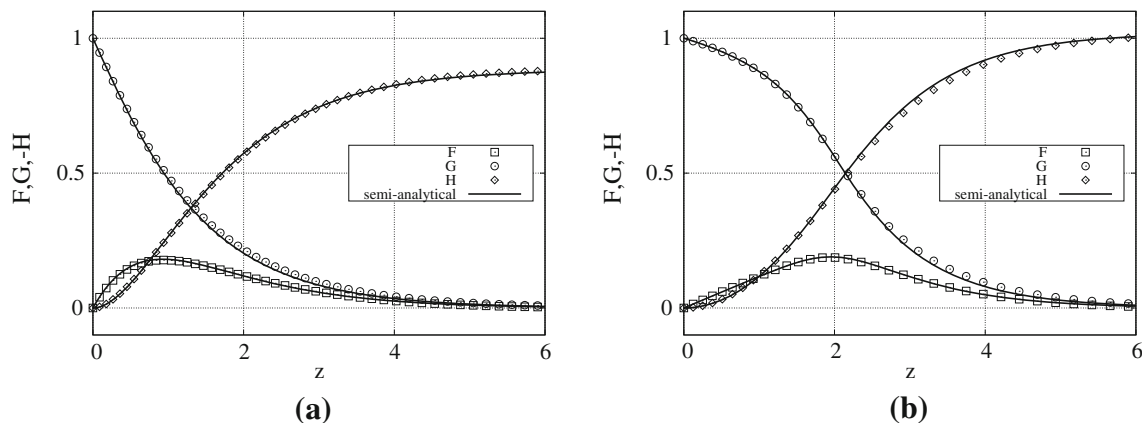

Fig. 8 Comparison between the velocity profiles F, G and H obtained by numerical integration of the generalized von Kármán equations (*continuous lines*) and by integration of the complete Navier–Stokes equations (*dots*), using the FEM. **a** Electrolyte with constant viscosity; **b** electrolyte viscosity depending on the z coordinate according to Eq. (79) with $v(z = 0)/v_\infty = 12$ and $q = 0.25$. Good agreement is obtained in both cases
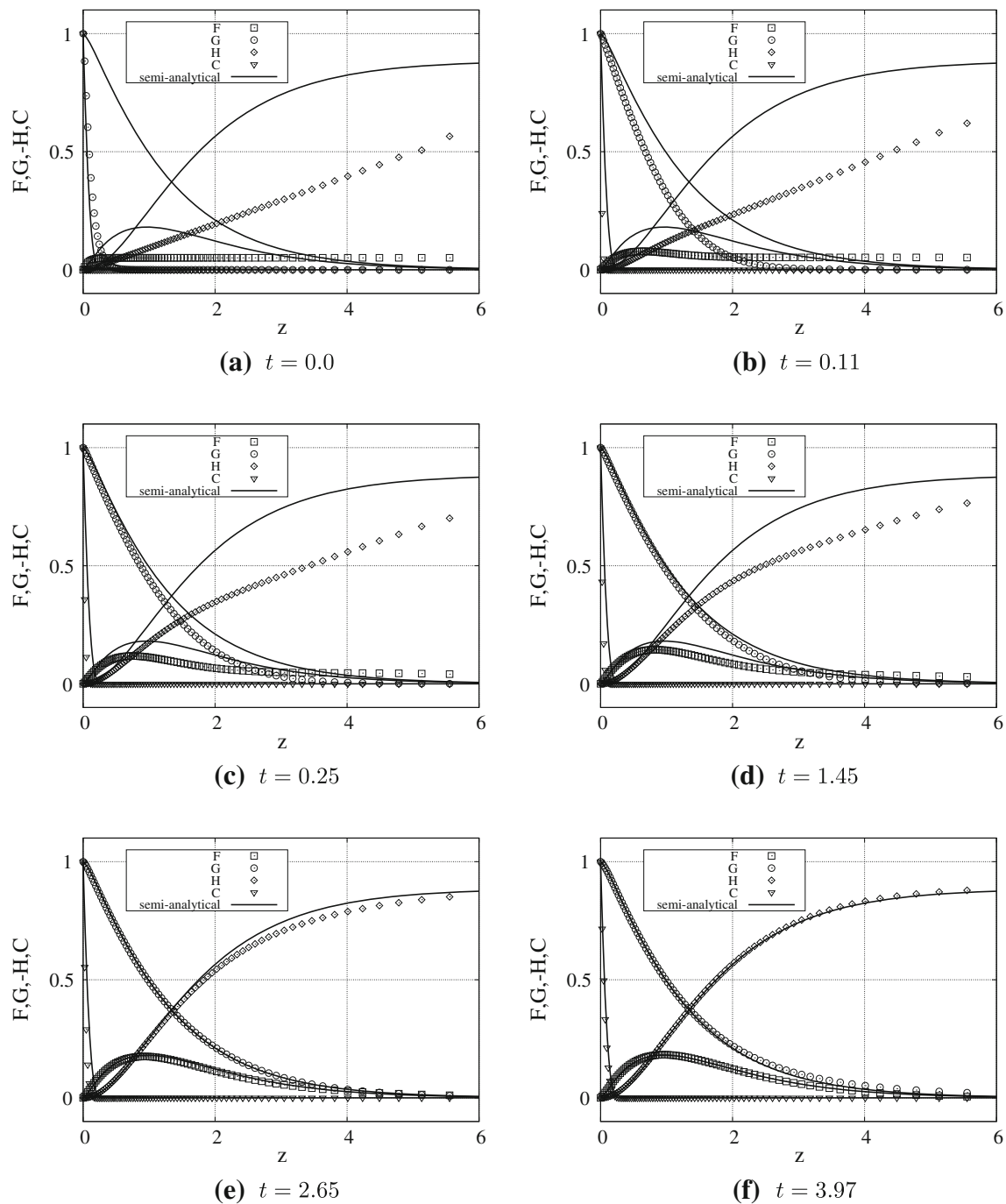
Fig. 9 Time evolution of the non-dimensionalized variables F, G, H and c for the solution of the Navier–Stokes equation coupled to the mass transport equation through the viscosity. The finite element method was used to discretize the equations and the mini element was chosen to fulfill the stability requirements of the Babuska–Brezzi condition [24]. *Continuous lines* refer to the solution of Eqs. (10–14), with the viscosity according to Eq. (6) and $\hat{v}_0/\hat{v}_\infty = 2.255$. Simulation time is non-dimensional

asymptotic approach to the steady-state solution. The initial condition of the system was set with the fluid at rest. The successive iteration of the numerical method clearly converges to the steady state (see Fig. 9f). The convergence of the final solution was monitored by the relative norm L_1 given by Eq. (78), thus the stationary solution was found when $L_1 < 1E - 06$.

The stationary solution of the numerical simulation of the rotating disk electrodes is thus compared to the generalized von Kármán's flow in Fig. 10. The mesh used in
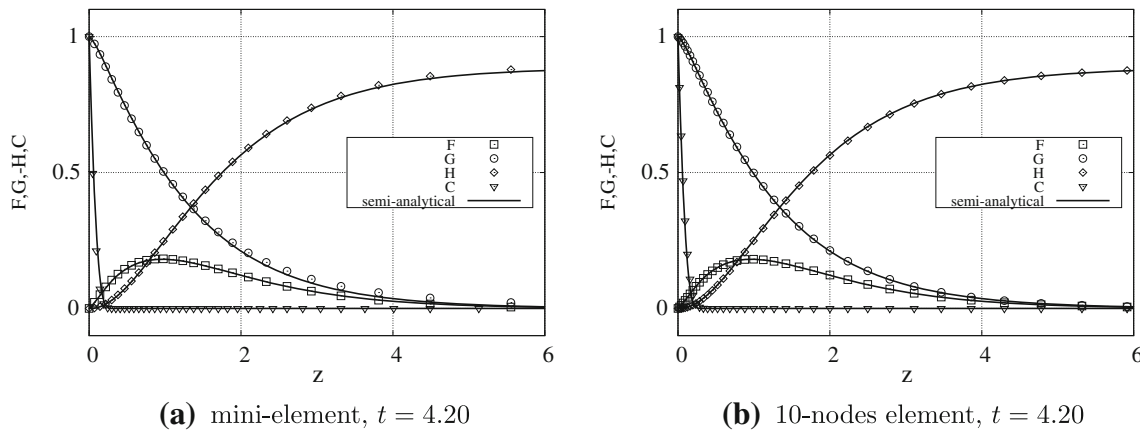
J Braz. Soc. Mech. Sci. Eng. (2014) 36:709–724

723

(a) mini-element, $t = 4.20$

(b) 10-nodes element, $t = 4.20$

Fig. 10 Non-dimensional profiles F, G H and C obtained by numerical integration of the generalized von Kármán equations (*continuous lines*) and by integration of the complete Navier–Stokes equations (*dots*), using the FEM with the **a** mini element and **b** 10-node tetrahedron. The electrolyte viscosity depends on the concentration of the chemical species according to Eq. (6). Good

agreement was obtained between the numerical simulation and the semi-analytical method for both elements. However, the numerical diffusion can be noted in the small offset of the profiles G and H for the mini element in $1.5 < z < 4.0$ with respect to the semi-analytical solution. Simulation time is non-dimensional

these two simulations comprised 130,080 vertices, and 740,625 elements using the mini element and the 10-node elements. The additional centroid in the mini element mesh led to a total of 870,705 nodes, while the additional mid-edge nodes in the 10-node element mesh presented a total of 1,013,784 nodes. As can be seen, good agreement was found between the numerical simulation and the semi-analytical solution of the rotating disk flow coupled with a mass transport equation for the mini and the 10-node elements. However, a small offset can be noticed for the numerical solution of the profiles G and H using the mini element (Fig. 10a). Such a discrepancy can be attributed to the numerical diffusion introduced by the mini element, due to the absence of second- and third-order terms in the interpolating polynomial of the mini element, which is of fourth order. The thin concentration boundary layer required dense distribution of points close to the rotating disk to achieve the solution with accuracy. It is important to note that the coupling between mass transport and momentum equations through viscosity affects the final solution of the velocity boundary layers, thus the concentration boundary layer must be accurately computed.

6 Conclusions

The validation results herein presented show that the proposed FEM scheme reproduces the solution of the generalized von Kármán's equations for rotating disk flow coupled through the viscosity, to the transport of a chemical species. The thin mass concentration boundary layer

resulting from a Schmidt number equal to 2,000 requires a much larger number of points than those used in simulations of constant viscosity flows.

Good agreement to the semi-analytical solution was obtained from the discretization of the numerical domain using the mini and 10-node finite elements. It was verified that the mini element presented higher numerical diffusion with respect to the 10-node element. Such a conclusion is in accordance to the literature of finite elements.

As observed for the two previous simulations with different finite elements in Fig. 10, the results found here to the coupled hydrodynamic case show, in addition to the velocity field, no dependence of the non-dimensional concentration profile along the radial coordinate.

The transient regime of the rotating disk has shown different time scales for velocity and mass concentration profiles. This can be attributed to the fact that the viscous term of the transport equation was divided by a much larger value compared to that in the Navier–Stokes's equations and thereby reducing the diffusion effects.

Future application of the validated code will be focused on the stability analysis of electrochemical cells, allowing an in-depth study on the dynamic of 3-dimensional perturbations in linear regime as well as saturation and interaction of modes within non-linear regimes.

References

1. Levich V (1962) Physicochemical hydrodynamics. Prentice-Hall, Englewood Cliffs, New Jersey

2. Barcia O, Mattos O, Tribollet B (1992) Anodic dissolution of iron in acid sulfate under mass transport control. J Electrochem Soc 139:446–453

3. Mangiavacchi N, Pontes J, Barcia OE, Mattos OE, Tribollet B (2007) Rotating disk flow stability in electrochemical cells: effect of the transport of a chemical species. Phys Fluids 19:114109

4. Hughes T, Franca L, Balestra M (1985) A new finite element formulation for computational fluid dynamics: V. circunventing the Babuska–Brezzi condition: a stable Petrov–Galerkin formulation of the stokes problem accomodating equal-order interpolations. Computer Methodos Appl Mech Eng 59:85–99

5. Hughes T, Franca L, Mallet M (1986) A new finite element formulation for computational fluid dynamics: I. Symmetric forms of the compressible euler and Navier–Stokes equation and the second law of thermodynamics. Computer Methodos Appl Mech Eng 54:223–34

6. Donea J (1984) A Taylor–Galerkin method for convective transport problems. Int J Num Methods Eng 20:101–19

7. Löhner R, Morgan K, Zienkiewicz O (1985) An adaptive finite element procedure for compressible high speed flows. Computer Methodos Appl Mech Eng 51:441–65

8. Oden J, Babuska I, Baumann C (1998) A discontinuous hp finite element method for diffusion problems. J Comput Phys 146:491–519

9. Baumann C, Oden J (1998) A discontinuous hp finite element method for convection–diffusion problems. Computer Methods Appl Mech Eng 175:311–341

10. Moisy F, Doaré O, Passuto T, Daube O, Rabaud M (2004) Experimental and numerical study of the shear layer instability between two counter-rotating disks. J Fluid Mech 507:175–202

11. Batchelor GK (1967) An introduction to fluid dynamics. Cambridge Mathematical Library, Cambridge University Press, New York

12. Barcia O, Mangiavacchi N, Mattos O, Pontes J, Tribollet B (2008) Rotating disk flow in electrochemical cells: a coupled solution for hydrodynamic and mass equations. J Eletrochem Soc 155:424–427

13. Hughes T, Brooks A (1982) A theoretical framework for Petrov-Galerkin methods with discontinuous weighting functions: application to the streamline upwind procedure. In: Gallagher RH, Norrie DM, Oden JT, Zienkiewicz OC (eds) Finite elements in fluids. Selected papers from the Third international conference on finite elements in flow problems, Canada, June 10–13, vol. 4. Wiley, New York

14. Wiin-Nielsen A (1959) On the application of trajectory methods in numerical forecasting. Tellus 11:180–196

15. Krishnamurti T (1962) Numerical integration of primitive equations by a quasi-Lagrangian advective scheme. J Appl Meteorol 1:508–521

16. Sawyer J (1963) A semi-Lagrangian method of solving the vorticity advection equation. Tellus 15:336–342

17. Robert A (1981) A stable numerical integration scheme for the primitive meteorological equations. Atmosphere Oceans 19:35–46

18. Pironneau O (1982) On the transport-diffusion algorithm and its applications to the Navier–Stokes equation. Numerische Mathematik 38:309–332

19. Durran D (1998) Numerical Methods for waves equations in geophysical fluid dynamics. In: Marsden JE et al. (eds) Text in applied mathematics, 1st edn. Springer, Berlin

20. Anjos G, Mangiavacchi N, Pontes J, Botelho C (2006) Modelagem numérica de escoamentos acoplados ao transporte de uma espécie química pelo método dos elementos finitos. In: ENCIT 2006—Congresso Brasileiro de Ciências Térmicas e Engenharia, Curitiba, Brazil

21. Anjos G, Mangiavacchi N, Pontes J, Botelho C (2006) Simulação numérica das equações de saint-venant utilizando o método dos elementos finitos. In: 16 POSMEC—Simpósio de Pós-Graduação em Engenharia Mecânica. Uberlândia, Brazil

22. Purser R, Leslie L (1996) Generalized Adams–Bashforth time integration schemes for a semi-Lagrangian model employing the second-derivative of the horizontal momentum equations. Quart J Royal Meteorol Soc 122:737–763

23. Cuvelier C, Segal A, van Steenhoven AA (1986) Finite element method and Navier–Stokes equations. Dordrecht, Holland

24. Zienkiewicz OC, Taylor RL (2000) The finite element method for fluids dynamics, 5th edn. Butterworth-Heinemann, Oxford

25. Oden JT, Carey G (1984) Finite elements: mathematical aspects. Texas finite element series, vol 4, Prentice-Hall, New Jersey

26. Hughes TJR (1987) The finite element method—linear static and dynamic finite element analysis. Dover civil and mechanical engineering. Dover Publications, New York

27. Zienkiewicz OC, Taylor RL (2000) The finite element method volume 1: the basis, 5th edn. Butterworth-Heinemann, Oxford

28. Chorin AJ (1968) Numerical solution of the Navier–Stokes equations. Math Comput 22:745–762

29. Patankar SV (1980) Numerical heat transfer and fluid flow. Hemisphere series on computational methods in mechanics and thermal science. Taylor & Francis, New York

30. Harlow FH, Welch JE (1965) Numerical calculation of time-dependent viscous incompressible flow of fluid with free surface. Phys Fluids 8:2182–2189

31. Lee M, Oh B, Kim Y (2001) Canonical fractional-step methods and consistent boundary conditions for the incompressible Navier–Stokes equations. J Comput Phys 168(1):73–100

32. Chang W, Giraldo F, Perot B (2002) Analysis of an exact fractional step method. J Comput Phys 180:183–199

33. Christov CI, Pontes J (2002) Numerical scheme for Swift-Hohenberg equation with strict implementation of Lyapunov functional. Math Computer Model 35:87–99

34. Pontes J, Mangiavacchi N, Conceição AR, Barcia OE, Mattos OE, Tribollet B (2004) Rotating disk flow stability in electrochemical cells: effect of viscosity stratification. Phys Fluids 16(3):707–716

35. Schlichting H (1960) Boundary layer theory. McGraw-Hill series in mechanical engineering. McGraw-Hill, New York